EEG reconstruction and skull conductivity estimation using a Bayesian model promoting structured sparsity

Facundo Costa, Hadj Batatia, Thomas Oberlin, Jean-Yves Tourneret

September 21, 2016

Abstract

M/EEG source localization is an open research issue. To solve it, it is important to have good knowledge of several physical parameters to build a reliable head operator. Amongst them, the value of the conductivity of the human skull has remained controversial. This report introduces a novel hierarchical Bayesian framework to estimate the skull conductivity jointly with the brain activity from the M/EEG measurements to improve the reconstruction quality. A partially collapsed Gibbs sampler is used to draw samples asymptotically distributed according to the associated posterior. The generated samples are then used to estimate the brain activity and the model hyperparameters jointly in a completely unsupervised framework. We use synthetic and real data to illustrate the improvement of the reconstruction. The performance of our method is also compared with two optimization algorithms introduced by Vallaghé *et al.* and Gutierrez *et al.* respectively, showing that our method is able to provide results of similar or better quality while remaining applicable in a wider array of situations.

1 INTRODUCTION

M/EEG source localization has been receiving an increasing amount of interest in the signal processing literature in the last decade. One of the most common models used to solve the

associated ill-posed problem is the distributed source model that represents the brain activity as a fixed number of dipoles distributed over the brain cortex [1, 2]. The relationship between the brain activity and the M/EEG measurements is expressed by the head operator matrix, that is calculated based on the shape and composition of the subject's head. Most of the techniques developed for M/EEG source localization rely on having precise knowledge about the head operator. However there are several factors that introduce uncertainty in its calculation, most noticeably the geometry and conductivity of the different tissues that compose the human head.

Several head models with varying precision and complexity have been used throughout the years, being mainly divided in two categories (1) the shell head models and (2) the realistic head models [2] that are represented in Fig. 1.1. The former model the human head using a fixed number of concentric spheres (typically 3 or 4). Each sphere represents the interface between two different tissues of the human head considered to be uniform with constant conductivities [3]. In the three-shell head model the skull, cerebrospinal fluid and brain tissues are considered whereas the four-shell model adds an additional outer-most sphere to model the head tissue. In order to calculate the head operator with the shell models it is necessary to set different parameters: (1) the radius of the spheres, (2) the conductivity of each tissue, (3) the amount and locations of the dipoles inside the brain and (4) the amount and locations of the electrodes in the scalp. On the other hand, the realistic head models are typically computed from the MRI of the patient in order to better represent the distribution of different tissues inside the human head. To perform this calculation it is possible to use several methods [2] including the boundary element method (BEM) [4], the finite element method (FEM) [5] and the finite difference method (FDM) [6]. However, in order to be able to compute a head model operator from the MRI it is still necessary to set several parameters including (1) the conductivity of each tissue, (2) the amount and locations of the dipoles inside the brain and (3) the amount and locations of the electrodes in the scalp.

Since the dipoles are only a discrete approximation of a continuous current distribution, their amount and positions inside the brain are arbitrary [1]. They are typically distributed uniformly inside the brain and the amount of dipoles is chosen depending on the desired resolution for the activity estimation. In contrast, the other parameters represent physical properties and should be set as close as possible to their real values in order to ensure the quality of the activity estimation. Considering this, several authors have analyzed the influence of these parameters in the estimation of brain activity. Minor errors in the electrode positions have been shown not to affect significantly the results [7] whereas there is a much higher sensibility to variations in the tissue conductivities, making their values critical [8–11]. The conductivities of the human head tissue, cerebrospinal fluid and brain have well known values that are accepted in the literature [8]. However, there has been some controversy regarding the conductivity of the human skull [2]. The ratio between scalp and skull conductivities was initially reported to be 80 [12] but since then other authors have published values as low as 15 [13]. The value of the human skull conductivity is also known to vary significantly across different subjects [2, 14]. Because of this, it remains of interest to develop methods that estimate the skull conductivity to improve the quality of the brain activity reconstruction. This can be done using techniques such as impedance tomography (EIT) [14], using intracranial electrodes [15] or measuring it directly during surgery [13]. However it is also possible to

estimate it directly from the M/EEG measurements, which is the objective of this paper. Several methods have been proposed to estimate the conductivity of the skull and the brain activity jointly, albeit requiring very restrictive conditions to yield good results. For instance, having a very good a-priori knowledge about the active dipole positions [16, 17], assuming there is only one dipole active [18] or limiting the estimation of the skull conductivity to a few discrete values [19, 20]. In [16] Gutierrez *et al* presented a method capable of estimating the activity amplitude jointly with the skull conductivity as long as the active dipoles are known in advance. The estimation is performed using a concentrated likelihood function that is used to find the maximum likelihood estimator (MLE) of the skull conductivity. Vallaghé *et al* [18] introduced an optimization method that estimates the location of one dipole jointly with the conductivities of the different tissues. More precisely, the dipole location and the conductivities were estimated iteratively using the MUSIC algorithm and the Nelder-Mead method.

This paper studies a method able to estimate the skull conductivity jointly with the M/EEG brain activity assuming focal point-like brain activity without requiring any additional prior information. The method is based on a hierarchical Bayesian model introduced in [21]. This model assigns a multivariate Bernoulli Laplacian prior to the brain activity to approximate an ℓ_{20} mixed norm regularization in order to reconstruct point-like brain activity by promoting structured sparsity. In the current work we generalize this model to estimate the skull conductivity jointly with the brain activity in a completely unsupervised framework. The posterior distribution of this generalized model is too complex to derive closed form expressions for the conventional Bayesian estimators of its unknown parameters. Consequently, a Markov chain Monte Carlo method is investigated to generate samples asymptotically distributed according to the posterior distribution of interest. These generated samples are then used to compute Bayesian estimators of the unknown model parameters and hyperparameters.

This paper is organized as follows: The joint EEG deconvolution and operator estimation problem is formulated in Section 2. The Bayesian model proposed to solve this problem is introduced in Section 3. Section 4 presents the partially collapsed Gibbs sampler that generates samples from the posterior distribution of the proposed model. The method used to model the operator dependency on the skull conductivity is presented in Section 5. Section 6 studies some interesting moves allowing the sampler convergence to be improved. Section 7 presents experimental results. Section 8 investigates how to asses the convergence, and Section 9 finally concludes the paper.

2 PROBLEM STATEMENT

We consider T time samples of M electrodes generated by N dipoles located in the surface of the brain cortex and oriented orthogonally to it. Motivations for this can be found in [1]. We generalize the model by considering that the operator depends on the skull conductivity

$$\boldsymbol{Y} = \boldsymbol{H}(\rho)\boldsymbol{X} + \boldsymbol{E} \tag{2.1}$$

(a) Shell model   (b) MRI Scan
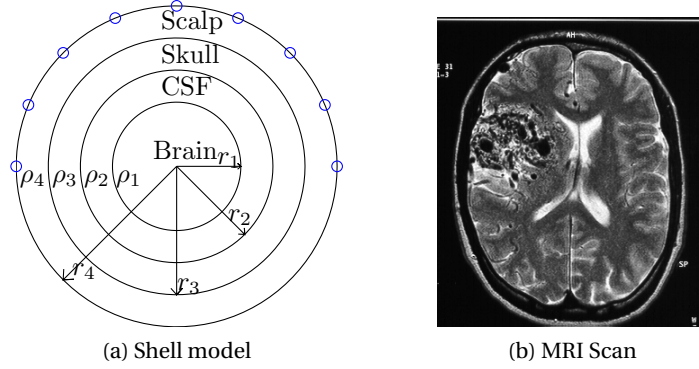
Figure 1.1: Shell and realistic brain model representations.

where the dipole amplitudes are represented by $X \in \mathbb{R}^{N \times T}$, $H(\rho) \in \mathbb{R}^{M \times N}$ is the lead field operator that varies with the skull conductivity, $Y \in \mathbb{R}^{M \times T}$ contains the electrode measurements and $E \in \mathbb{R}^{M \times T}$ is the measurement noise.

The problem addressed in this work is the joint estimation of the matrix X and the conductivity ρ from the measurement matrix Y using a parametric form for the operator H depending on the conductivity ρ.

2.1 OPERATOR NORMALIZATION

The depth biasing effect is a well known problem when solving the M/EEG source localization by minimizing a certain norm of the solution [1]. This effect is caused by the fact that each active dipole generates a signal whose amplitude is varying from one dipole to another. It is possible to compensate for this effect by either: (1) adding a weight vector v with elements $v_i = |h^i|_2$ that penalize the dipoles associated with large M/EEG measurements or (2) normalizing the columns of the operator so that they all have a unitary norm. When using the second option, the EEG source localization problem can be written as

$$Y = \bar{H}(\rho)\bar{X} + E \tag{2.2}$$

where the columns of the normalized operator are $\bar{h}^i = \frac{h^i}{|h^i|_2}$ and the rows of the estimated activity are $\bar{x}_i = |h^i|_2 x_i$ being m^i the i-th column of matrix M and m_i its i-th row. Since our model has a variable operator, using the first approach would cause the weight vector v to depend on the skull conductivity ρ which introduces unnecessary complexities. To avoid these, we use the second compensation model.

3 PROPOSED HIERARCHICAL BAYESIAN MODEL

3.1 LIKELIHOOD

We assume an independent white Gaussian noise with a constant variance σ_n^2, which leads to the following Gaussian likelihood

$$f(\boldsymbol{Y}|\bar{\boldsymbol{X}},\sigma_n^2,\rho) = \prod_{t=1}^{T} \mathcal{N}\left(\boldsymbol{y}^t \middle| \bar{\boldsymbol{H}}(\rho)\bar{\boldsymbol{x}}^t, \sigma_n^2 \mathbb{I}_M\right) \tag{3.1}$$

where $\mathbb{I}_M$ is the identity matrix of size $M \times M$. Note that if the noise cannot be assumed to be white, it is possible to estimate the noise covariance from the measurements and use it to whiten the data [22].

3.2 PRIOR DISTRIBUTIONS

The dependencies between the different model parameters and hyperparameters after the introduction of the latent variable τ^2 (that simplifies sampling) is shown in Fig. 3.1. The priors used for each of them (apart from the skull conductivity ρ) are the same that were used in the ℓ_{20} model of [21] with $\nu_i = 1$ (due to the operator normalization described in Section 2.1) and are summarized in Table 3.1. The reader is invited to consult [21] for motivations and more details about our original model. The prior used for the skull conductivity is introduced in Section 3.2.1.
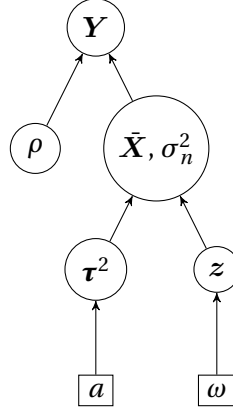

Figure 3.1: Directed acyclic graph for the proposed Bayesian model.

z_i	$\mathcal{B}\left(z_i|\omega\right)$	
τ_i^2	$\mathcal{G}\left(\tau_i^2 \middle| \frac{T+1}{2}, \frac{a}{2}\right)$	
$\bar{x}_i$	$\delta(\bar{x}_i)$	if $z_i = 0$
	$\mathcal{N}\left(0, \sigma_n^2 \tau_i^2 \mathbb{I}_T\right)$	if $z_i = 1$
σ_n^2	$\frac{1}{\sigma_n^2} 1_{\mathbb{R}^+}(\sigma_n^2)$	
a	$\mathcal{G}\left(a \middle| \alpha, \beta\right)$	
ω	$\mathcal{U}\left(\omega \middle| 0, 1\right)$	

Table 3.1: Prior distributions $f(z_i|\omega)$, $f(\tau_i^2|a)$, $f(\bar{x}_i|z_i, \tau_i^2, \sigma_n^2)$, $f(\sigma_n^2)$, $f(a)$ and $f(\omega)$.

where $1_{\mathbb{R}^+}(x)$ if $x \in \mathbb{R}^+$ and 0 otherwise and $\alpha = \beta = 1$.

3.2.1 SKULL CONDUCTIVITY

In order to keep the model simple we propose to assign a non-informative uniform prior for the skull conductivity

$$f(\rho) = \mathcal{U}\left(\rho \middle| \rho_{\min}, \rho_{\max}\right). \tag{3.2}$$

To select the range of this uniform distribution we consider an interval containing the scalp-to-skull conductivity ratios reported in the literature [12, 23], i.e, defined by $r_{\min} = 10$ and $r_{\max} = 100$. Considering the scalp conductivity to be $330\frac{mS}{m}$, this leads to $\rho_{\min} = 3.3\frac{mS}{m}$ and $\rho_{\max} = 33\frac{mS}{m}$.

3.3 POSTERIOR DISTRIBUTION

The corresponding posterior distribution is defined as follows

$$f(\boldsymbol{Y}, \sigma_n^2, \bar{\boldsymbol{X}}, \boldsymbol{z}, a, \boldsymbol{\tau}^2, \omega, \rho) \propto f(\boldsymbol{Y}|\bar{\boldsymbol{X}}, \sigma_n^2, \rho) f(\bar{\boldsymbol{X}}|\boldsymbol{\tau}^2, \boldsymbol{z}, \sigma_n^2) f(\boldsymbol{z}|\omega) f(\boldsymbol{\tau}^2|a) f(\sigma_n^2) f(a) f(\omega) f(\rho) \tag{3.3}$$

4 PARTIALLY COLLAPSED GIBBS SAMPLER

Unfortunately, the posterior distribution (3.3) is intractable and does not allow to express estimators of the different parameters and hyperparameters to be expressed in closed-form. As a consequence, we propose to draw samples from (3.3) and use them to estimate the brain activity jointly with the model hyperparameters. More precisely, we investigate a partially collapsed Gibbs sampler that samples the variables z_i and x_i jointly in order to exploit the strong correlation between these two variables. Denoting as $\boldsymbol{X}_{-i}$ the matrix $\boldsymbol{X}$ whose ith row has been replaced by zeros, the proposed sampler samples the different variables according to their conditional distributions as shown in Algorithm 1.

The corresponding conditional distributions are summarized in Table 4.1 and the next subsection. Their exact derivation can be found in an appendix of [21]. Note that the only difference between this sampler and the sampler of [21] is the last line in which the skull conductivity is sampled.

Algorithm 1 Partially Collapsed Gibbs sampler.

Initialize all the parameters.
repeat
  for $i = 1$ to N **do**
    Sample τ_i^2 from $f(\tau_i^2|\bar{x}_i, \sigma_n^2, a, z_i)$
    Sample z_i from $f(z_i|Y, \bar{X}_{-i}, \sigma_n^2, \tau_i^2, \omega, \rho)$
    Sample $\bar{x}_i$ from $f(\bar{x}_i|z_i, Y, \bar{X}_{-i}, \sigma_n^2, \tau_i^2, \rho)$
  end for
  Sample a from $f(a|\boldsymbol{\tau}^2)$
  Sample σ_n^2 from $f(\sigma_n^2|Y, \bar{X}, \boldsymbol{\tau}^2, z, \rho)$
  Sample ω from $f(\omega|z)$
  Sample ρ from $f(\rho|\bar{X}, Y, \sigma_n^2)$
until convergence

τ_i^2	$\mathcal{G}\left(\frac{T+1}{2}, \frac{a}{2}\right)$ if $z_i = 0$ $\mathcal{GIG}\left(\frac{1}{2}, a, \frac{\|x_i\|^2}{\sigma_n^2}\right)$ if $z_i = 1$
z_i	$\mathcal{B}\left(1, \frac{k_1}{k_0+k_1}\right)$
x_i	$\delta(x_i)$ if $z_i = 0$ $\mathcal{N}\left(\boldsymbol{\mu}_i, \sigma_i^2\right)$ if $z_i = 1$
a	$\mathcal{G}\left(\frac{N(T+1)}{2} + \alpha, \frac{\sum_i \tau_i^2}{2} + \beta\right)$
σ_n^2	$\mathcal{IG}\left(\frac{(M+\|z\|_0)T}{2}, \frac{1}{2}\left[\|\bar{H}(\rho)X - Y\|^2 + \sum_i \frac{\|x_i\|^2}{\tau_i^2}\right]\right)$
ω	$\mathcal{B}e\left(1 + \|z\|_0, 1 + N - \|z\|_0\right)$

Table 4.1: Conditional distributions $f(\tau_i^2|x_i, \sigma_n^2, a, z_i)$, $f(z_i|Y, X_{-i}, \sigma_n^2, \tau_i^2, \omega, \rho)$, $f(x_i|z_i, Y, X_{-i}, \sigma_n^2, \tau_i^2, \rho)$, $f(a|\boldsymbol{\tau}^2)$, $f(\sigma_n^2|Y, X, \boldsymbol{\tau}^2, z, \rho)$ and $f(\omega|z)$.

with

$$\boldsymbol{\mu}_i = \frac{\sigma_i^2 \bar{h}(\rho)^{i\,T}(Y - \bar{H}(\rho)X_{-i})}{\sigma_n^2}, \sigma_i^2 = \frac{\sigma_n^2 \tau_i^2}{1 + \tau_i^2 \bar{h}(\rho)^{i\,T} \bar{h}(\rho)^i}$$

$$k_0 = 1 - \omega, k_1 = \omega \left(\frac{\sigma_n^2 \tau_i^2}{\sigma_i^2}\right)^{-\frac{T}{2}} \exp\left(\frac{\|\boldsymbol{\mu}_i\|^2}{2\sigma_i^2}\right).$$

4.1 CONDITIONAL DISTRIBUTION OF ρ

The following conditional distribution of the skull conductivity can be written

$$f(\rho|\bar{X}, Y, \sigma_n^2) \propto \exp\left(-\frac{\|\bar{H}(\rho)\bar{X} - Y\|^2}{2\sigma_n^2}\right) 1_{[\rho_{\min}, \rho_{\max}]}(\rho). \tag{4.1}$$
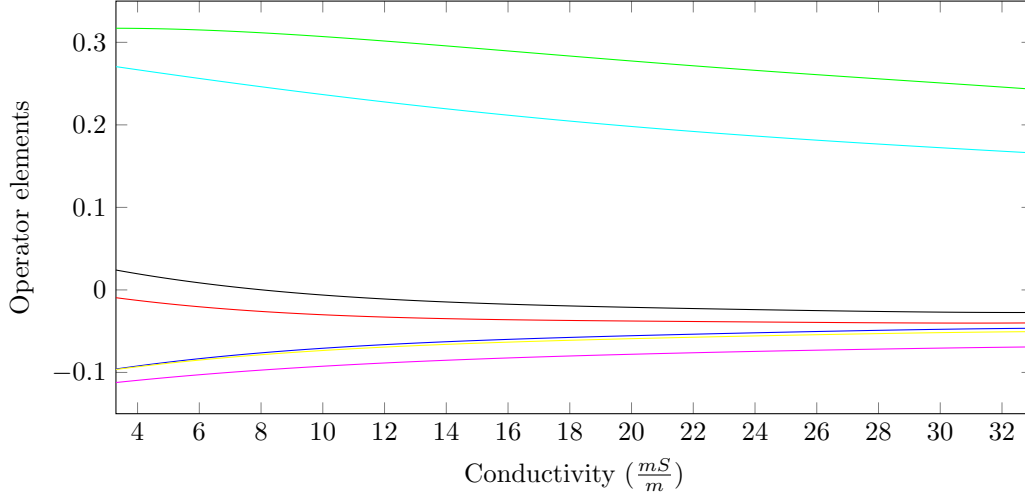
Figure 5.1: Variations of operator elements with respect to ρ.

For arbitrary functions $\bar{\boldsymbol{H}}(\rho)$, (4.1) does not belong to a common family of distributions. The following section explains how to efficiently model the operator $\bar{\boldsymbol{H}}(\rho)$ and to sample from (4.1).

5 OPERATOR MODEL

5.1 DEPENDENCY

Shell models can be used to derive closed form expressions for $\bar{\boldsymbol{H}}(\rho)$. However these models are quite complex [2] and would make the sampling from $f(\rho|\bar{\boldsymbol{X}}, \boldsymbol{Y}, \sigma_n^2)$ considerably difficult. In contrast, realistic head models can be calculated numerically for particular values of ρ but do not provide a closed-form expression for $\bar{\boldsymbol{H}}(\rho)$. In order to illustrate how the value of ρ affects the operator, a four-shell 200-dipole head model with 41 electrodes was calculated for different values of ρ. Eight elements of the operator $h_{i,j}(\rho)$ (chosen randomly) are displayed in Fig. 5.1 as a function of ρ. In order to have a simple expression of this dependency, Şengül *et al* [17] proposed to replace $\bar{\boldsymbol{H}}(\rho_k)$ by its linearization around the current value ρ_k. This method was shown to provide good results but requires evaluating the exact value $\bar{\boldsymbol{H}}(\rho)$ every iteration which slows down the algorithm considerably. Since the variation of the operator elements with respect to ρ is smooth and monotonic, we propose to approximate $\bar{\boldsymbol{H}}(\rho)$ using a simple mathematical expression as in [17]. However, the approximation is computed on the whole range $\rho_{\min} < \rho < \rho_{\max}$ with a polynomial matrix of small degree denoted by $\hat{\boldsymbol{H}}(\rho)$. This allows us to have a simple closed form expression of $\hat{\boldsymbol{H}}(\rho)$ for both shell and realistic head models. In addition, our method only requires calculating the exact $\bar{\boldsymbol{H}}(\rho)$ to construct the polynomial matrix $\hat{\boldsymbol{H}}(\rho)$ offline, after which only the polynomial matrix is evaluated accelerating the iteration speed considerably.

5.2 CONSTRUCTION OF THE APPROXIMATED MATRIX $\hat{\boldsymbol{H}}(\rho)$ WITH A POLYNOMIAL INTERPOLATION

Each element of $\hat{\boldsymbol{H}}(\rho)$ is constructed as a polynomial function of ρ

$$\hat{h}_{i,j}(\rho) = \sum_{l=0}^{L} c_{i,j,l}\rho^l. \tag{5.1}$$

We propose to calculate the coefficients $c_{i,j,l}$ using polynomial least-squares fitting. This consists in minimizing the following mean square error between $\bar{\boldsymbol{H}}(\rho)$ and $\hat{\boldsymbol{H}}(\rho)$

$$\sum_{k=0}^{K-1} \left(\bar{h}_{i,j}(\rho_k) - \sum_{l=0}^{L} c_{i,j,l}\rho_k^l \right)^2 \tag{5.2}$$

Note that the exact value of $\bar{\boldsymbol{H}}(\rho)$ is calculated for $\rho_k = \rho_{\min} + \frac{k(\rho_{\max}-\rho_{\min})}{K-1}$ with $0 \le k \le K-1$ by either using the shell model expression [3] or by evaluating numerically the head model from the patient's MRI [4]. After this we calculate the polynomial coefficients $c_{i,j,l}$ that minimize (5.2) that are

$$\boldsymbol{c}_{i,j} = \left[\sum_{k=0}^{K-1} \boldsymbol{\psi}_k \boldsymbol{\psi}_k^T \right]^{-1} \sum_{k=0}^{K-1} \bar{h}_{i,j}(\rho_k)\boldsymbol{\psi}_k \tag{5.3}$$

being $\boldsymbol{\psi}_k = [\rho_k^0, ..., \rho_k^L]^T$ and $\boldsymbol{c}_{i,j} = [c_{i,j,0}, ..., c_{i,j,L}]^T$.
The next section will discuss how to sample the skull conductivity after the coeficients $c_{i,j,l}$ have been calculated.

5.3 SAMPLING THE SKULL CONDUCTIVITY

Approximating the relationship between the operator and the skull conductivity with a polynomial matrix allows us to have a simple closed form expression for $f(\rho|\bar{\boldsymbol{X}}, \boldsymbol{Y}, \sigma_n^2)$

$$f(\rho|\bar{\boldsymbol{X}}, \boldsymbol{Y}, \sigma_n^2) \propto \exp\left(-g(\rho) \right) 1_{[\rho_{\min}, \rho_{\max}]}(\rho) \tag{5.4}$$

where $g(\rho) = \frac{||\hat{\boldsymbol{H}}_{L,K}(\rho)\bar{\boldsymbol{X}} - \boldsymbol{Y}||^2}{2\sigma_n^2}$ is a polynomial of order $2L$.
Since it is not easy to sample from (5.4) directly, we propose to adopt a random-walk Metropolis-Hastings (MH) move. More precisely, this move consists in proposing a new sample $\rho_{\text{prop}} = \rho_{\text{old}} + \epsilon$ and accepting it with probability

$$P_{acc} = \begin{cases} \min\left(\frac{\exp(-g(\rho_{prop}))}{\exp(-g(\rho_{old}))}, 1 \right) & \text{if } \rho_{\min} < \rho_{\text{prop}} < \rho_{\max} \\ 0 & \text{otherwise.} \end{cases} \tag{5.5}$$

We propose to use a zero-mean Gaussian distribution for the random walk noise ϵ, i.e., $f(\epsilon) = \mathcal{N}(0, \sigma_\epsilon^2)$. The variance of the random walk σ_ϵ^2 was adjusted empirically in order to obtain an appropriate acceptance rate, as recommended in [24]. Based on our experiments performed in Section 7, we set $\sigma_\epsilon = \frac{\rho_{\max}-\rho_{\min}}{100}$.

6 CONVERGENCE DIAGNOSIS

6.1 MULTIPLE DIPOLE SHIFT PROPOSALS

As noticed in our previous work [21], the Gibbs sampler presented above tends to gets stuck around local maxima of the posterior distribution. In particular, the variable z does not usually converge to indicate the correct positions of the active dipoles in a reasonable amount of time. To solve this problem we introduced in [21] multiple dipole shift proposals allowing D random non-zeros to be moved to neighboring positions. These moves are accepted or rejected using the classical MH acceptance rate.

Algorithm 2 Multiple dipole shift proposal.

$\hat{z} = z$
repeat D times
    Set ind_{old} to be the index of a random non-zero of z
    Set $p = [\text{ind}_{\text{old}}, \text{neigh}_{\gamma,\rho}(\text{ind}_{\text{old}})]$
    Set ind_{new} to be a random element of p
    Set $\hat{z}_{\text{ind}_{\text{old}}} = 0$ and $\hat{z}_{\text{ind}_{\text{new}}} = 1$
end
Sample $\hat{\rho}$ from $f(\hat{\rho}|Y, \sigma_n^2, \tau^2, \hat{z})$.
Sample $\hat{X}$ from $f(\hat{X}|\hat{z}, Y, \sigma_n^2, \tau^2, \hat{\rho})$.
Sample $\hat{\tau}^2$ from $f(\hat{\tau}^2|\hat{X}, \sigma_n^2, a, \hat{z})$.
Set $\{z, \tau^2, \rho\} = \{\hat{z}, \hat{\tau}^2, \hat{\rho}\}$ with probability $\min\left(\frac{f(\hat{z}, \hat{\tau}^2, \hat{\rho}|Y, a, \sigma_n^2, \omega)}{f(z, \tau^2, \rho|Y, a, \sigma_n^2, \omega)}, 1\right)$
Else, do not change the values of $\{z, \tau^2, \rho\}$
Resample X if the proposed move has been accepted

In order to build more efficient proposals, we expand the multiple dipole shift moves to include the skull conductivity ρ. We do this by adding a step to sample the skull conductivity ρ marginally to X. The final algorithm is illustrated in Algorithm 2 where we define the neighborhood of each dipole as

$$\text{neigh}_{\gamma,\rho}(i) \triangleq \{j \neq i \mid |\text{corr}(\hat{h}(\rho)^i, \hat{h}(\rho)^j)| \geq \gamma\} \tag{6.1}$$

where $\hat{h}(\rho)^i$ is the ith column of $\hat{H}(\rho)$, $\gamma \in [0,1]$ tunes the neighborhood size ($\gamma = 0$ corresponds to a neighborhood containing all the dipoles and $\gamma = 1$ corresponds to an empty neighborhood). The values of D and γ were adjusted by cross validation to $D = 2$ and $\gamma = 0.8$. To accept or reject the moves introduced before, we need to evaluate the distribution $f(z, \tau^2, \rho|Y, a, \sigma_n^2, \omega)$ up to a multiplicative constant. Considering only the values of the subset of z that change between the current value and the proposal (denoted by r) and applying the arithmetic manipulations detailed in [21], the following result can be obtained

$$f(z_r, \tau_r^2, \rho|Y, a, \sigma_n^2, \omega) \propto (1-\omega)^{C_0} \omega^{C_1} (\sigma_n^2)^{-\frac{TC_1}{2}} |\Sigma|^{\frac{T}{2}} \prod_{i \in I_1} (\tau_i^2)^{-\frac{T}{2}} \exp\left(-\frac{\sum_{t=1}^{T} Q^t}{2}\right) \prod_{i=1}^{N} \mathscr{G}\left(\tau_i^2 \middle| \frac{T+1}{2}, \frac{a}{2}\right) \tag{6.2}$$

where $\boldsymbol{I}_j = \{i | z_{r_i} = j\}$, C_j is the cardinal of the set $\boldsymbol{I}_j$ (for $j = \{0, 1\}$) and

$$\Sigma^{-1} = \frac{1}{\sigma_n^2} \left[\boldsymbol{H}^{\boldsymbol{I}_1}(\rho)^T \boldsymbol{H}^{\boldsymbol{I}_1}(\rho) + \text{diag}\left(\frac{1}{\tau_r^2}\right) \right]$$

$$\mu^t = -\frac{\Sigma \boldsymbol{H}^{\boldsymbol{I}_1}(\rho)^T [\boldsymbol{H}^{-r}(\rho) \boldsymbol{x}_{-r}^t - \boldsymbol{y}^t]}{\sigma_n^2}$$

$$Q^t = \frac{[\boldsymbol{H}^{-r}(\rho) \boldsymbol{x}_{-r}^t - \boldsymbol{y}^t]^T [\boldsymbol{H}^{-r}(\rho) \boldsymbol{x}_{-r}^t - \boldsymbol{y}^t]}{\sigma_n^2} - \mu^{t^T} \Sigma^{-1} \mu^t$$

with diag($\boldsymbol{s}$) the diagonal square matrix formed by the elements of the vector $\boldsymbol{s}$.

6.2 INTER-CHAIN PROPOSALS

As explained in our previous work [21], when running multiple MCMC chains in parallel it is possible for the different chains to get stuck around different values of $\boldsymbol{z}$. As a consequence, inter-chain proposals can be considered to improve the sampler convergence. These proposals were exchanging active dipoles of different chains, with a probability defined according to the MH acceptance rate.

Algorithm 3 Inter-chain proposals.

Define a vector $\boldsymbol{c} = \{1, ..., L\}$ where L is the number of chains
for $i = \{1, 2, ..., L\}$
    Choose (and remove) a random element from $\boldsymbol{c}$ and denote it by k
    Denote as $\{\hat{z}_k, \hat{\boldsymbol{\tau}}_k^2, \hat{\rho}_k\}$ the sampled values of $\{\boldsymbol{z}, \boldsymbol{\tau}^2, \rho\}$ for the MCMC chain #k
    For the chain #i set $\{\boldsymbol{z}_i, \boldsymbol{\tau}_i^2, \rho_i\} = \{\hat{z}_k, \hat{\boldsymbol{\tau}}_k^2, \hat{\rho}_k\}$ with probability $\frac{f(\hat{z}_k, \hat{\boldsymbol{\tau}}_k^2, \hat{\rho}_k|.)}{f(\boldsymbol{z}, \boldsymbol{\tau}^2, \rho|.)}$
    Resample $\boldsymbol{X}$ if the proposal has been accepted
end

We now expand the inter-chain proposals to include the conductivity ρ to improve the sampling efficiency. More precisely, at each iteration, an exchange between the active dipoles of random pairs of chains is proposed with probability π (the value of π was fixed to 10^{-3} by crossvalidation) and this exchange is accepted with the MH probability as shown in Algorithm 3.

7 EXPERIMENTAL RESULTS

7.1 SYNTHETIC DATA

Synthetic data is first considered using a 200-dipole Stok four-sphere head model [3] with 41 electrodes. The dipoles were uniformly distributed in the brain cortex oriented orthogonally to the brain surface. Two different kinds of activations are investigated: (1) single dipole activations with low SNR and (2) multiple dipole activations with high SNR. Before applying our method to the data we will evaluate the sensitivity of the method to the values of K and L.

7.1.1 SELECTION OF K AND L

In order to construct $\hat{\boldsymbol{H}}(\rho)$ we have to select appropriate values for K and L. Increasing the values of K and L clearly improves the quality of the approximation of $\hat{\boldsymbol{H}}$ at the price of higher computational complexity. To choose appropriate values for K and L, it is interesting to analyze their effect on the estimation of ρ when all the other parameters ($\boldsymbol{X}$ and σ_n^2) are known. To do this we will use several ground truth values of $\boldsymbol{X}$ and σ_n^2 and consider that the algorithm would ideally converge to the value $\hat{\rho}$ that minimizes the polynomial of order $2L$ defined as $g(\rho) = \frac{||\hat{\boldsymbol{H}}_{L,K}(\rho)\bar{\boldsymbol{X}} - \boldsymbol{Y}||^2}{2\sigma_n^2}$.
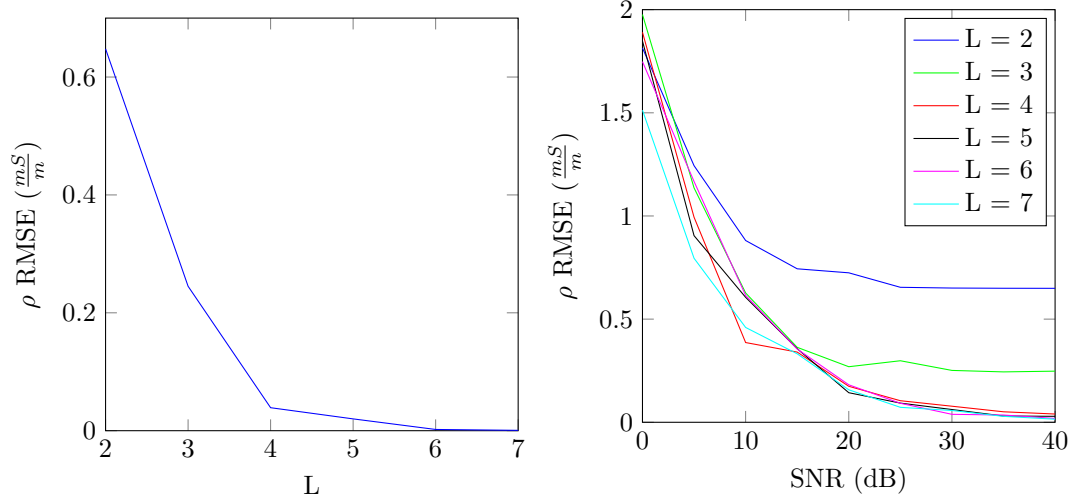
Using the head model described in the previous subsection, we used $K = 100$ and generated values of L in the range $2 \leq L \leq 7$. We also considered ten different ground truth values of ρ_{gt}, 200 different values of $\bar{\boldsymbol{X}} \in \mathbb{R}^{200 \times 100}$ (each of them having one of the 200 dipoles with a constant activity during the 100 time samples) and 9 values of SNR (from 0dB to 40dB in steps of 5dB) resulting in a total of 108.000 experiments. Since the ground truth $\bar{\boldsymbol{X}}$ is used for the estimation of $\hat{\rho}$, the only factors that explain the difference between $\hat{\rho}$ and ρ_{gt} are the presence of noise and the approximation of $\bar{\boldsymbol{H}}(\rho)$ by $\hat{\boldsymbol{H}}_L(\rho)$, which allows us to illustrate the effect of L for different values of SNR. We define the root mean square error of the estimation of ρ for a particular value of L and SNR as

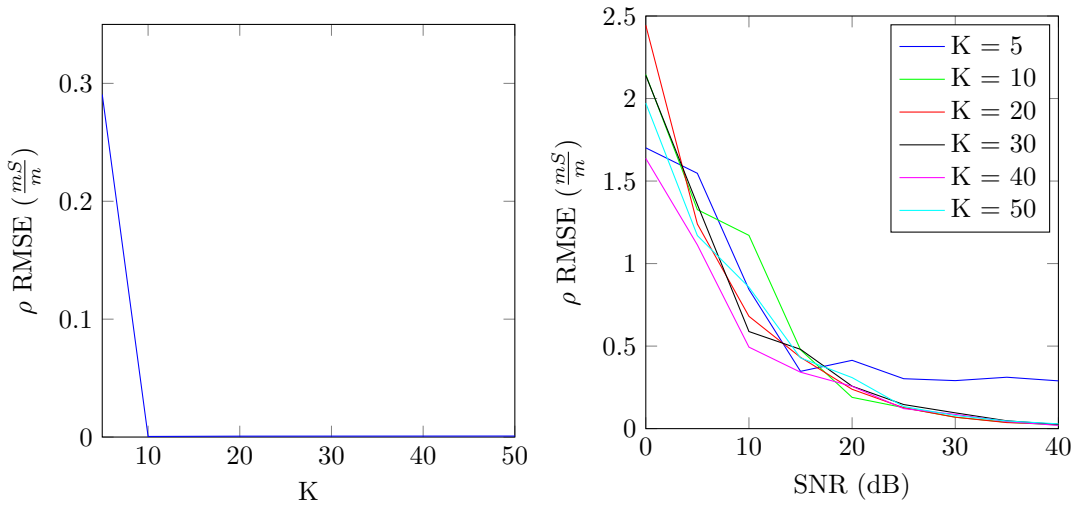$$RMSE(L, SNR) = \sqrt{\frac{1}{200 \times 10} \sum_{i=1}^{200 \times 10} (\hat{\rho}_i - \rho_i)^2} \tag{7.1}$$

ρ_i being the ground truth of ρ for the ith realization obtained for the specified values of L and SNR and $\hat{\rho}_i$ the corresponding estimated value of ρ.

Fig. 7.1(a) illustrates the RMSE of the estimation of ρ as a function of SNR for each value of L and for noiseless simulations. We can see that in noiseless situations, the error seems to tend asymptotically to 0 as the value of L increases, as expected. However, when the measurements are noisy the minimum value of RMSE is limited by the amount of noise. For instance, if the measurements have an SNR of 10dB the estimation error only decreases until $L = 3$. This shows that for high SNR it makes sense to choose a high value of L but for common values of SNR (lower than 20dB) choosing high values of L does not improve the quality of the estimation of ρ. Because of this, for a given SNR, we choose the smallest value of L such that $|RMSE(SNR, L+1) - RMSE(SNR, L)| < \epsilon$.

To analyze the effect of K, the same experiment was performed by varying $K \in \{5, 10, 20, 30, 40\}$ and fixing $L = 5$ for $K = 5$ and $L = 7$ for the higher values of K. Fig. 7.1(b) shows the RMSE of ρ for noisy and noiseless simulations. Both figures show that there is a significant improved approximation when K is increased from 5 to 10 if the SNR is high enough. However, choosing values of K higher than 10 does not improve the estimation of the skull conductivity ρ. Since we will be working with values of SNR between 10 and 30dB we have decided to use $L = 4$ and $K = 10$ in the rest of the paper.

(a) RMSE of ρ VS L (K = 100). Noiseless (left) and noisy (right) measurements.

(b) RMSE of ρ VS K (L = 7). Noiseless (left) and noisy (right) measurements.

Figure 7.1: Root mean square error of the skull conductivity estimation

(a) Histograms of a, ω, σ_n^2 and ρ for the proposed model (ρ estimated).

(b) Histograms of a, ω and σ_n^2 for the default-ρ model ($\rho = \rho_{fix}$ is not estimated)
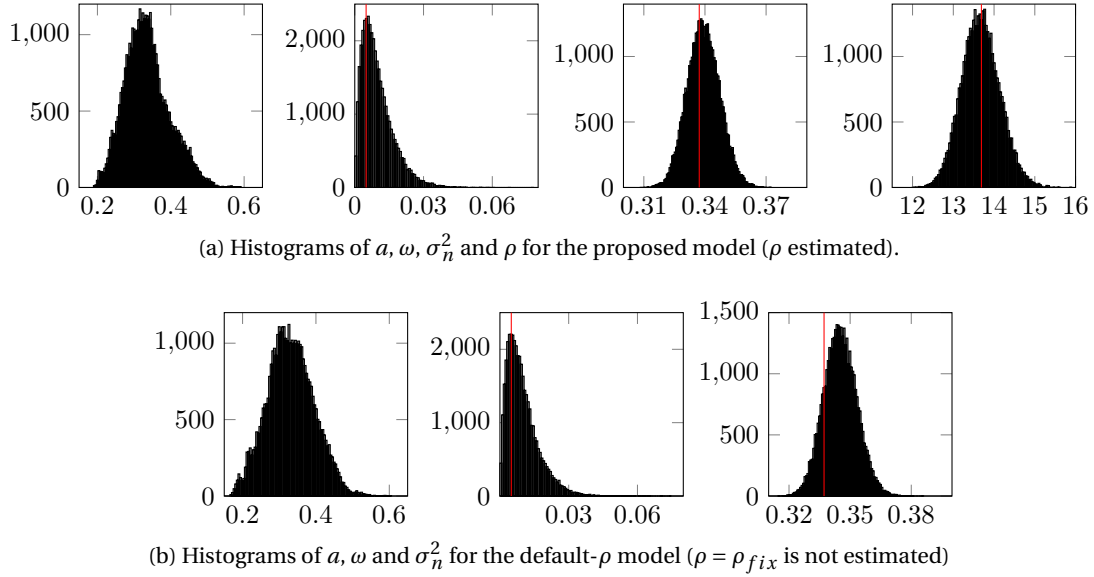
Figure 7.2: Estimated posterior distribution of the model parameters for simulation #1 (single dipole)

7.1.2 SINGLE DIPOLE ACTIVATIONS

In the first kind of simulations, a random single dipole was assigned a damped sine activation of 5Hz. The activation was sampled at 200Hz and multiplied with the head operator with a chosen ground truth value of ρ denoted as ρ_{gt}. Gaussian white noise was added to the measurements to have a signal to noise ratio $SNR = 10$dB. The proposed estimation method is compared with two other methods: (1) a variation of the proposed method that uses a fixed value of the conductivity, more precisely $\rho_{fix} = \frac{\rho_{max} + \rho_{min}}{2} = 18.15 \frac{mS}{m}$ in order to illustrate the advantages of estimating ρ (called default-ρ model) and (2) the optimization method studied by Vallaghé *et al* [18] that is able to estimate ρ and the brain activity jointly if there is only one active dipole. Both the proposed model and the default-ρ model use 8 parallel MCMC chains. We illustrate two different cases. The first case corresponds to a conductivity ρ_{gt} close to ρ_{fix} (simulation #1) and the second case is characterized by a higher difference between ρ_{gt} and ρ_{fix} (simulation #2). More precisely, $\rho_{gt} = 13.68 \frac{mS}{m}$ for simulation #1 and $\rho_{gt} = 3.59 \frac{mS}{m}$ for simulation #2.

For simulation #1, all methods manage to find the active dipole in its exact location. The histograms of the simulated parameters for the two Bayesian models (corresponding to a fixed value of ρ and to an unknown value of ρ respectively) are shown in Fig. 7.2. First we comment the results obtained with the proposed model and its default-ρ variation. In order to understand why the model with a fixed value of ρ is able to correctly recover the activation despite the use of a wrong operator, it is important to note on the different histograms that the proposed model is able to estimate all variables correctly. Note also that the default-ρ model seems to overestimate the noise variance σ_n^2. Thus, when the difference between the operators is small, the default-ρ model is able to mitigate the effect of a wrong operator by
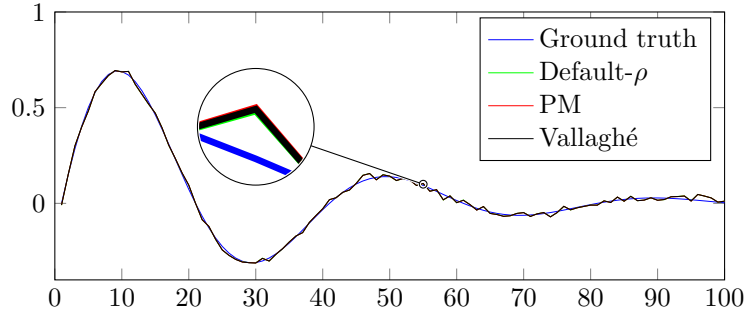
Figure 7.3: Recovered waveforms in the single dipole simulation #1.

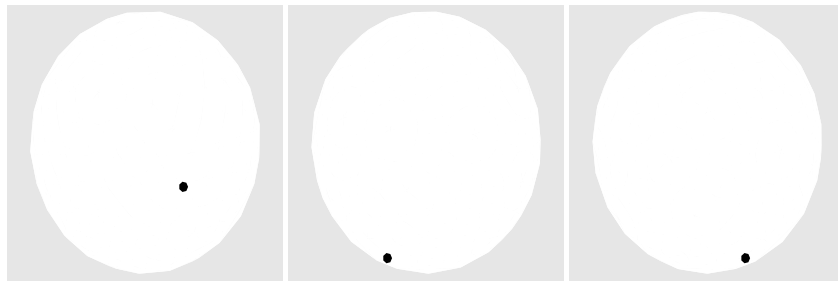considering that there is additional noise in the system.

Vallaghé's optimization method also estimates the dipole location correctly for simulation #1. After running simulation #1 for 20 Monte Carlo runs with different values of noise, the mean estimate value of the skull conductivity was $\hat{\rho} = 13.63\frac{mS}{m}$ (which is very close to the actual ground truth value $13.69\frac{mS}{m}$). The proposed method is able to estimate the posterior distribution of the skull conductivity (as shown in Fig. 7.2). This distribution can be used to determine the MMSE estimator of ρ (the mean of the posterior distribution, that is $13.64\frac{mS}{m}$) as well as uncertainties regarding this estimator. For instance the standard deviation of the MMSE estimator is $0.46\frac{mS}{m}$. Since the proposed method is not restricted to a point-estimate as Vallaghé's optimization method, it is not necessary to run different Monte Carlo runs for different values of noise.

Finally, Fig. 7.3 compares the estimated waveforms obtained with the proposed method (PM) and Vallaghés one, where we can observe that both estimated waveforms are close to the ground truth. Quantitative results associated with simulation #1 are summarized in Table 7.1.
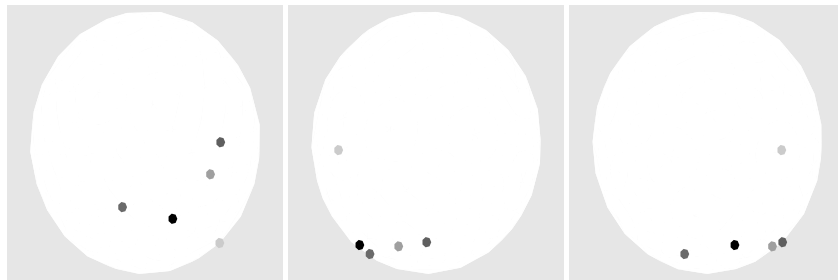
The estimated locations for simulation #2 are shown in Fig. 7.4. In this case the default-ρ model fails to recover the correct dipole location and spreads the activity over a significant area of the brain, due to the fact that the difference between the operators is significantly higher. The optimization method is still able to recover the dipole position correctly and gives an average estimate of the skull conductivity $\hat{\rho} = 3.85\frac{mS}{m}$ over 20 Monte Carlo runs while the proposed method estimates a mean value of $3.49\frac{mS}{m}$ (closer to the ground truth value of $3.59\frac{mS}{m}$) with a standard deviation of $0.12\frac{mS}{m}$. Fig. 7.5 shows that in this case the proposed method estimates a waveform that is considerably closer to the ground truth. Table 7.2 summarizes quantitative results of simulation #2.

The price to pay with the good performance of the proposed method is its computational complexity. Using Matlab implementations in a modern Xeon CPU E3-1240 processor, each simulation was processed on average in 96.1 seconds by the proposed model, 51.29 seconds by the default-ρ model and 23.8 seconds by Vallaghé's method. This is a common disadvantage of Bayesian methods when compared with optimization techniques.
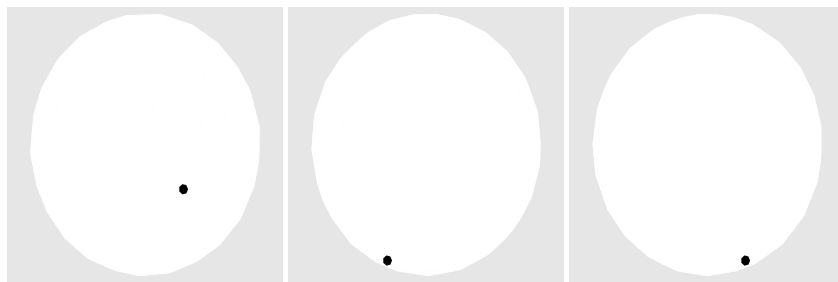
In summary, both the proposed and Vallaghé's method are able to find the correct dipole position for both simulations but the proposed method is able to better estimate the skull
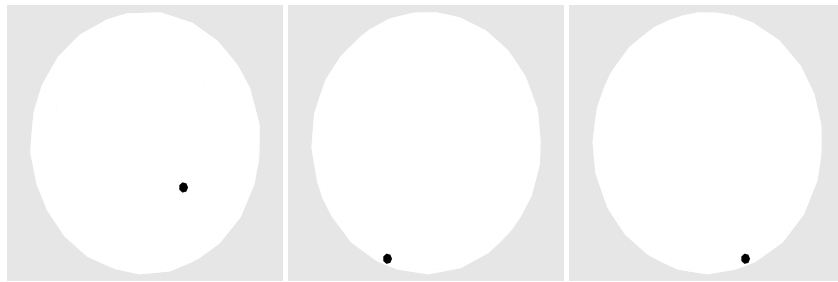
(a) Ground truth - Axial, coronal and sagittal views respectively

(b) Default-ρ model - Axial, coronal and sagittal views respectively

(c) Proposed method - Axial, coronal and sagittal views respectively

(d) Vallaghé's method - Axial, coronal and sagittal views respectively

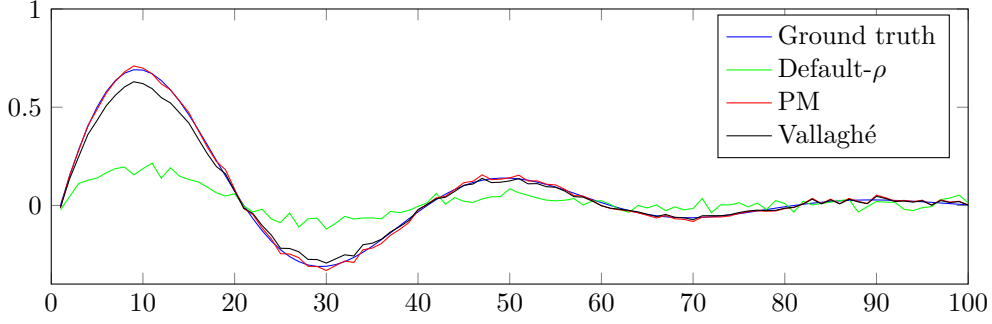Figure 7.4: Estimated activity for single dipole simulation #2.

Figure 7.5: Estimated waveforms for simulation #2 (single dipole)

Method	Position error	$\frac{\|\hat{X}-X_{gt}\|_F^2}{\|X_{gt}\|_F^2}$	$\frac{\hat{\sigma}_n{}^2-\sigma_n^2}{\sigma_n^2}$	$\hat{\rho}-\rho_{gt}$	$\frac{\|\boldsymbol{H}(\rho_{gt})-\boldsymbol{H}(\hat{\rho})\|_F^2}{\|\boldsymbol{H}(\rho_{gt})\|_F^2}$
Default-ρ	0	2.53×10^{-3}	26.99×10^{-3}	4.46×10^{-3}	2.51×10^{-3}
PM	0	2.47×10^{-3}	6.21×10^{-3}	-43.89×10^{-6}	1.21×10^{-6}
Vallaghé	0	128×10^{-6}	N/A	-52.83×10^{-6}	1.15×10^{-6}

Table 7.1: Estimation errors for the different parameters (Simulation #1)

conductivity and the activation waveforms for simulation #2 while not being restricted to single dipole activations as Vallaghé's method.

7.1.3 MULTIPLE DIPOLE ACTIVATIONS

The second kind of simulations considered a variable amount of active dipoles to analyze the detection capabilities of the algorithm. In each simulation, C dipoles were activated with damped sinusoidal waves with frequencies varying between 5 and 20Hz. The activations were sampled at 200Hz and scaled in amplitude in order to produce the same energy in the different measurements. Twenty different simulations where conducted for each value of $C = 1, ..., 16$, each one having a different set of active dipoles and a different uniform random value of conductivity in the range $\rho_{\min} < \rho_{gt} < \rho_{\max}$, resulting in a total of 320 experiments. Noise was added to the measurements to obtain SNR = 30dB.

Since Vallaghé's method cannot be applied to activations that have more than a single active dipole the performance of the proposed model was compared with two other recovery methods: (1) the correct-ρ model with $\rho_{fix} = \rho_{gt}$ (to evaluate the loss of performance when

Method	Position error	$\frac{\|\hat{X}-X_{gt}\|_F^2}{\|X_{gt}\|_F^2}$	$\frac{\hat{\sigma}_n{}^2-\sigma_n^2}{\sigma_n^2}$	$\hat{\rho}-\rho_{gt}$	$\frac{\|\boldsymbol{H}(\rho_{gt})-\boldsymbol{H}(\hat{\rho})\|_F^2}{\|\boldsymbol{H}(\rho_{gt})\|_F^2}$
Default-ρ	224×10^{-3}	1.36	108.4×10^{-3}	14.56×10^{-3}	75.85×10^{-3}
PM	0	2.47×10^{-3}	5.89×10^{-3}	10.33×10^{-6}	77.14×10^{-9}
Vallaghé	0	6.17×10^{-3}	N/A	265×10^{-6}	92.3×10^{-6}

Table 7.2: Estimation errors for the different parameters (Simulation #2)

(a) Recovery rate versus C.

(b) Proportion of residual energy versus C.

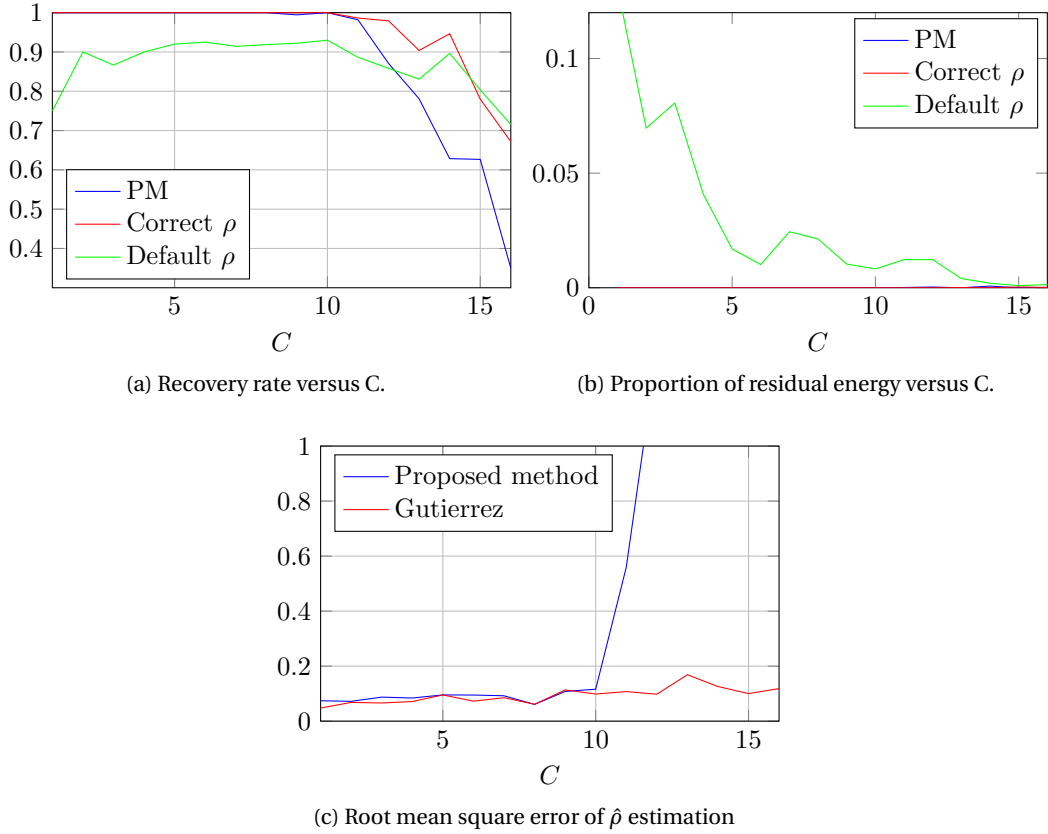(c) Root mean square error of $\hat{\rho}$ estimation

Figure 7.6: Performance measures for the estimation of multiple dipoles as a function of C.

ρ is estimated) and (2) a default-ρ model with a $\rho_{fix} = \frac{\rho_{\min} + \rho_{\max}}{2} = 18.15 \frac{mS}{m}$ (to illustrate the improvement due to the estimation of ρ). All models were run using 8 MCMC parallel chains. For each simulation result, the C estimated active dipoles that generated the strongest measurements in $\boldsymbol{Y}$ were considered to be the main dipoles recovered by the algorithm, while the other dipoles were used to compute the residual activity.

We define the recovery rate as the proportion of active dipoles that were recovered by a given method. Fig. 7.6(a) displays the average recovery rate as a function of C for the three models. The correct-ρ model is able to correctly recover the dipoles perfectly up to 10 dipoles, whereas its performance declines significantly when $C > 10$. The fact that the recovery performance decreases with more active non-zeros is well known since the operator span limits the maximum possible amount of non-zeros that can be recovered correctly [25]. In comparison, the proposed model is able to estimate ρ jointly with the brain activity up to $C = 10$ practically without any recovery loss. For $C > 10$ its performance decreases faster than the other method because of the increasing error in the estimation of ρ (as shown in Fig. 7.6(c)). The recovery rate of the default-ρ model is significantly worse than the proposed method even for low values of C for the same reasons mentioned for single dipoles. Since the recovery rate only considers the main detected dipoles, it is also interesting to analyze the energy

(a) Default-ρ model   (b) ℓ_{21} mixed norm   (c) Proposed method
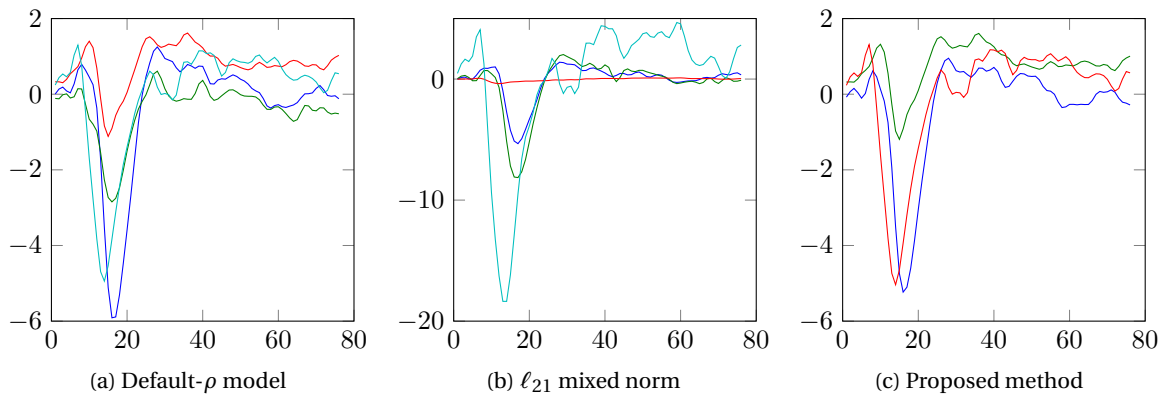
Figure 7.7: Estimated waveforms for the auditory evoked responses.

contained in the residual dipoles as well. Thus, we define the proportion of residual energy as the amount of energy contained in the measurements generated by the residual activity over the total energy in the measurements. This quantity is displayed in Fig. 7.6(b) where we can see that both the correct-ρ model and the proposed method have almost-zero energy (lower than 1%) in the residual dipoles for low values of C contrary to the default-ρ model that has a larger proportion of residual energy.

Our algorithm was also compared with Gutierrez' method [16] which estimates the activity amplitude jointly with the skull conductivity but requires knowing which are the active dipoles in advance. Because of this limitation, it makes no sense to analyze the recovery rate of Gutierrez' method but we can use it to compare the estimation of ρ as shown in Fig. 7.6(c). We can see that the estimation of both methods is comparable up to $C = 10$ despite the fact that our algorithm is able to estimate the active dipoles positions as well. For $C > 10$ the performance of our algorithm drops because it fails to recover the active dipole positions correctly.

In summary, upto $C = 10$ the quality of the reconstruction of the proposed method is very close to the method that knows the correct value of ρ in advance and significantly better than the default-ρ model and the error in the estimation of ρ is very close to the one of Gutierrez' method (that knows the active dipole positions in advance). For $C > 10$ the performance of the proposed method drops faster than the method that knows the ground truth value of ρ since the error in the estimation of ρ increases considerably.

7.2 REAL DATA

7.2.1 AUDITORY EVOKED RESPONSES

The left-ear auditory pure-tone stimulus data set from the MNE software [26, 27] was first investigated. It uses a realistic BEM (Boundary element method) head model containing 1.844 dipoles located on the cortex with orientations that are normal to the brain surface. The data was sampled with 306 MEG sensors at 600Hz, low-pass filtered at 40Hz and downsampled

19

(a) Default-ρ model

(b) ℓ_{21} mixed norm

(c) Proposed method

Figure 7.8: Estimated activity for the auditory evoked responses.

(a) Waveform 1 (Center right dipole)   (b) Waveform 2 (Center left dipole)   (c) Waveform 3 (Posterior left dipole)
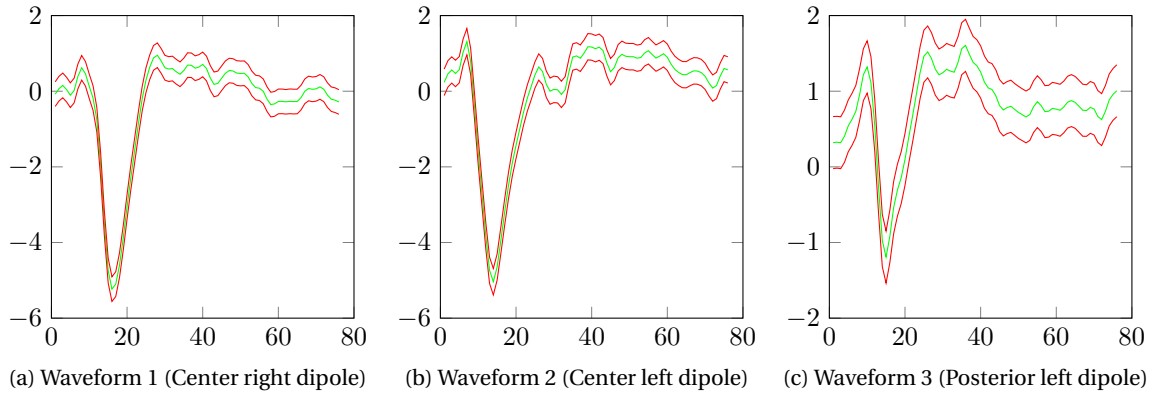
Figure 7.9: Estimated waveforms mean and boundaries $\mu \pm 2\sigma$ for the auditory evoked responses using the proposed model.

to 150Hz. One channel that had technical artifacts was ignored. The measurements corresponding to 200ms of data preceding each stimulus were considered to estimate the noise covariance matrix that was used to whiten the measurements. Fifty-one epochs were averaged to calculate Y. The activity of the source dipoles was estimated jointly with the skull conductivity for the period lasting 500ms after the stimulus. From a clinical perspective it is expected to find the brain activity primarily focused on the auditory cortices that are located close to the ears in both hemispheres of the brain.

The proposed method was compared with (1) a default-ρ model that uses $\rho = 6\frac{mS}{S}$, which is the value corresponding to a ratio of 50 between the scalp and skull conductivities). It is the default value used by the MNE software, and (2) the ℓ_{21} mixed norm regularization introduced in [22] also using an operator with $\rho = 6\frac{mS}{S}$.

We can see in Fig. 7.8 that out of the three models, the solution found by our method is the one that best agrees with the clinically expected solution of finding the activity focused on the auditory cortices whereas the other two spread the activity over several dipoles around the area. In addition, the MMSE estimator of the skull conductivity is $\hat{\rho} = 10.6\frac{mS}{S}$, corresponding to a ratio of 31 between the scalp and skull conductivities. This shows that this ratio is considerably lower than the value of 80 typically used in earlier research [12], in agreement with recent studies [13, 23].

The estimated waveforms are presented in Fig. 7.7: all methods estimate very similar waveforms. However, the proposed method concentrates the activity of several dipoles in the same one. The different waveforms detected by our algorithm are presented separately in Fig. 7.9 where the mean value for each activation and the confidence intervals for 2 standard deviations are displayed. We can see that the two dipoles located in the auditory cortices have most of their activity concentrated in strong peaks located around 90 ms after the stimulus, as it is clinically expected. The histograms of the sampled variables are shown in Fig. 7.10.

In summary, the proposed method is able to concentrate the brain activity more strongly in the auditory cortices (where it is expected to be) than the other two and estimates a value of ρ that is more compatible with the findings of recent studies than the default value used by
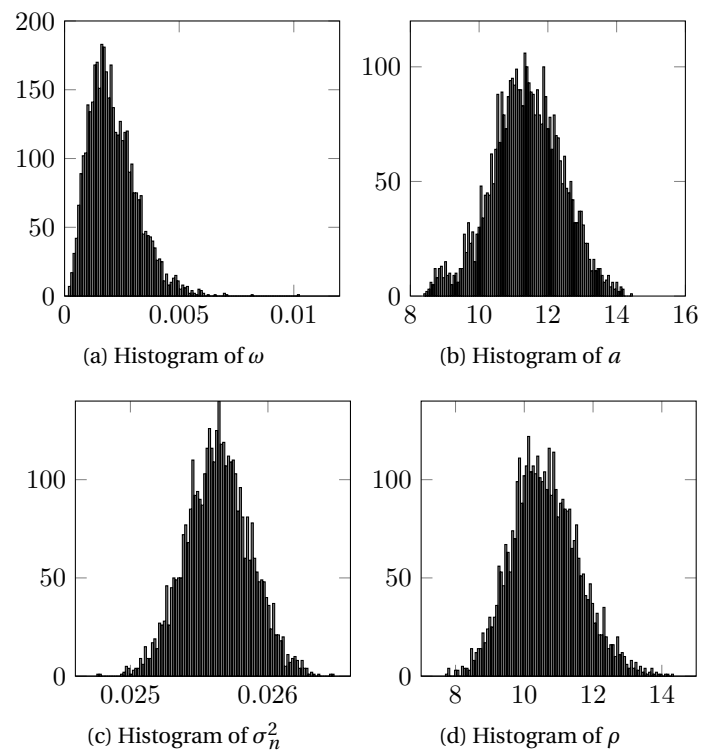
(a) Histogram of ω

(b) Histogram of a

(c) Histogram of σ_n^2

(d) Histogram of ρ

Figure 7.10: Hyperparameter histograms for the auditory evoked responses.

(a) PSRF of a

(b) PSRF of ω

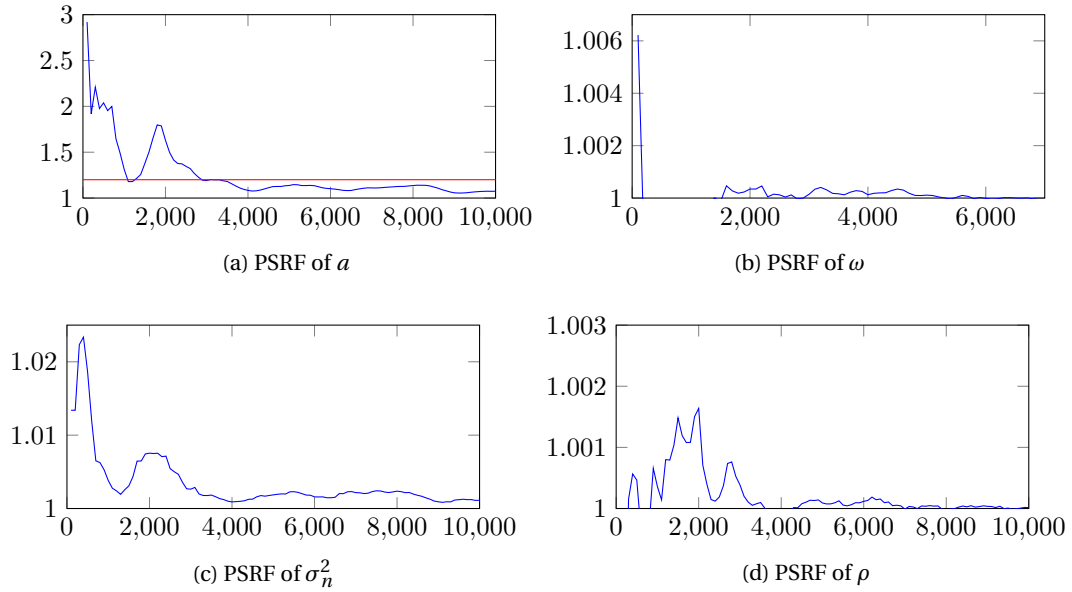(c) PSRF of σ_n^2

(d) PSRF of ρ

Figure 8.1: PSRFs for the proposed method along the iterations for simulation #1 (single dipole). Red line marks the 1.2 value that is typically considered the maximum acceptable value of PSRF that allows to conclude the simulation has converged.

the MNE software.

8 CONVERGENCE ASSESSMENT

In order to asses the convergence of the previous experiments, the Potential Scale Reduction Factors (PSRFs) [28] were considered. For single dipole simulation #1, the PSRFs of the different values are displayed in Fig. 8.1. Fig. 8.2 shows the PSRFs for the auditory evoked responses real data set. In both cases we can see that they tend to 1, showing the good numerical convergence of the proposed partially collapsed Gibbs sampler.

9 CONCLUSION

This paper introduced a novel Bayesian framework for sparse M/EEG reconstructions that is able to estimate the skull conductivity jointly with the underlying brain activity by using structured sparsity-promoting priors for the brain activity. A partially collapsed Gibbs sampler was used to generate samples from the posterior distribution that were used to estimate the model parameters and hyperparameters in a completely unsupervised framework. A polynomial approximation of the leadfield operator was used to reduce the computational cost of the sampling method used to sample the skull conductivities. The results of the proposed method were compared with the ones obtained with a fixed-conductivity model, showing that the proposed model is able to better estimate the underlying brain activity since this
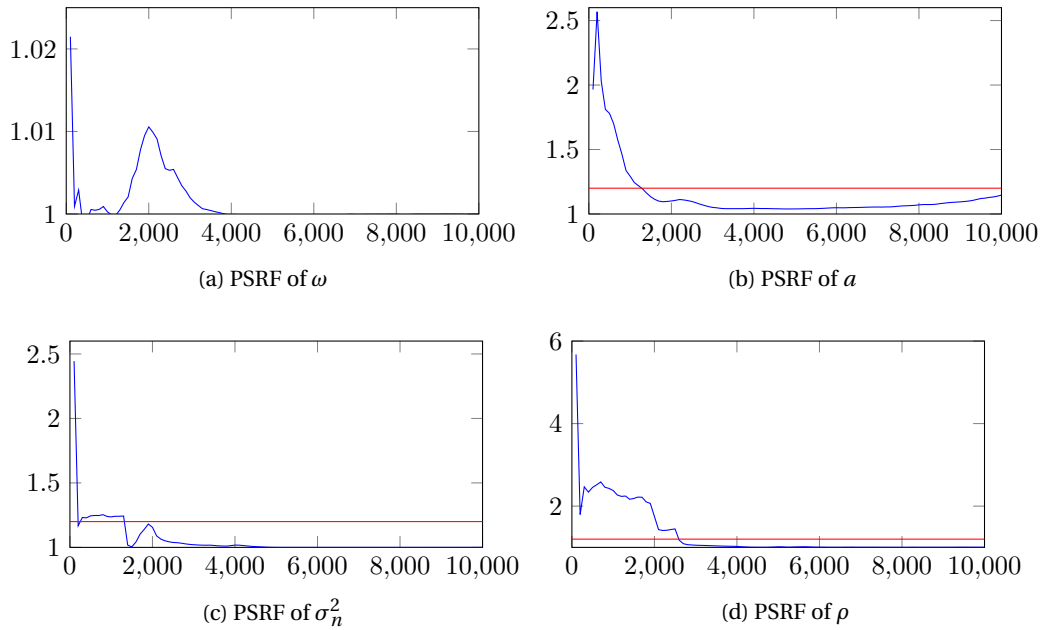
Figure 8.2: PSRFs of sampled variables for the auditory evoked responses along iterations. Red line marks the 1.2 value that is typically considered the maximum acceptable value of PSRF that allows to conclude the simulation has converged.

activity is estimated jointly with the skull conductivity. This improved performance was particularly observed when the value of skull conductivity used in the fixed-conductivity model was far away from its ground truth value or in the presence of multiple dipoles. In addition, the proposed method was compared to two different optimization techniques introduced by Vallaghé *et al* [18] and by Gutierrez *et al* [16]. Our method was shown to provide results of similar or better quality without requiring a single active dipole or knowledge of the active dipole positions in advance. Our algorithm was to an auditory evoked response real data set, showing that estimating the skull conductivity improves the quality of the reconstruction both when compared with the fixed-conductivity model and with the ℓ_{21} mixed norm regularization. Future work may changing the MCMC sampling to approximate message passing to reduce the computational complexity of the method.

REFERENCES

[1] R. Grech, T. Cassar, J. Muscat, K. P. Camilleri, S. G. Fabri, M. Zervakis, P. Xanthopoulos, V. Sakkalis, and B. Vanrumste, "Review on solving the inverse problem in EEG source analysis," *J. Neuroeng. Rehabil.*, vol. 4, pp. 5–25, 2008.

[2] H. Hallez, B. Vanrumste, R. Grech, J. Muscat, W. De Clercq, A. Vergult, Y. D'Asseler, K. P. Camilleri, S. G. Fabri, S. Van Huffel, et al., "Review on solving the forward problem in EEG source analysis," *J. Neuroeng. Rehabil.*, vol. 4, pp. 46–75, 2007.

[3] C. J. Stok, *The inverse Problem in EEG and MEG with Application to Visual Evoked Responses*, Ph.D. thesis, Univ. Twente, Enschede, The Netherlands, 1986.

[4] B. He, T. Musha, Y. Okamoto, S. Homma, Y. Nakajima, and T. Sato, "Electric dipole tracing in the brain by means of the boundary element method and its accuracy," *IEEE Trans. Biomed. Eng.*, vol. 34, no. 6, pp. 406–414, 1987.

[5] C. R. Johnson, *Numerical methods for bioelectric field problems*, Boca Rato (FL): CRC Press, 1995.

[6] F. Marino, E. Halgren, J.-M. Badier, M. Gee, and V. Nenov, "A finite difference model of electric field propagation in the human head: Implementation and validation," in *Proc. of the 19th Annual Northeast Bioengineering Conference*, New Jersey, USA, 1993, IEEE, pp. 82–85.

[7] Y. Wang and J. Gotman, "The influence of electrode location errors on EEG dipole source localization with a realistic head model," *Clin. Neurophys.*, vol. 112, no. 9, pp. 1777–1780, 2001.

[8] Z. A. Acar and S. Makeig, "Effects of forward model errors on EEG source localization," *Brain Topogr.*, vol. 26, no. 3, pp. 378–396, 2013.

[9] S. Vallaghé and M. Clerc, "A global sensitivity analysis of three-and four-layer EEG conductivity models," *IEEE Trans. Biomed. Eng.*, vol. 56, no. 4, pp. 988–995, 2009.

[10] B. Vanrumste, G. Van Hoey, R. Van de Walle, M. D'havé, I. Lemahieu, and P. Boon, "Dipole location errors in electroencephalogram source analysis due to volume conductor model errors," *Med. Biol. Eng. Comput.*, vol. 38, no. 5, pp. 528–534, 2000.

[11] N. G. Gençer and C. E. Acar, "Sensitivity of EEG and MEG measurements to tissue conductivity," *Phys. Med. Biol.*, vol. 49, no. 5, pp. 701, 2004.

[12] L. Geddes and L. Baker, "The specific resistance of biological material - a compendium of data for the biomedical engineer and physiologist," *Med. Biol. Eng. Comput.*, vol. 5, no. 3, pp. 271–293, 1967.

[13] R. Hoekema, G. Wieneke, F. Leijten, C. Van Veelen, P. Van Rijen, G. Huiskamp, J. Ansems, and A. Van Huffelen, "Measurement of the conductivity of skull, temporarily removed during epilepsy surgery," *Brain Topogr.*, vol. 16, no. 1, pp. 29–38, 2003.

[14] S. Gonçalves, J. C. De Munck, J. Verbunt, F. Bijma, R. M. Heethaar, F. Lopes da Silva, et al., "In vivo measurement of the brain and skull resistivities using an EIT-based method and realistic models for the head," *IEEE Trans. Biomed. Eng.*, vol. 50, no. 6, pp. 754–767, 2003.

[15] Y. Lai, W. Van Drongelen, L. Ding, K. Hecox, V. Towle, D. Frim, and B. He, "Estimation of in vivo human brain-to-skull conductivity ratio from simultaneous extra-and intra-cranial electrical potential recordings," *Clin. Neurophys.*, vol. 116, no. 2, pp. 456–465, 2005.

[16] D. Gutiérrez, A. Nehorai, and C. H. Muravchik, "Estimating brain conductivities and dipole source signals with EEG arrays," *IEEE Trans. Biomed. Eng.*, vol. 51, no. 12, pp. 2113–2122, 2004.

[17] G. Şengül and U. Baysal, "An extended Kalman filtering approach for the estimation of human head tissue conductivities by using EEG data: a simulation study," *Physiol. Meas.*, vol. 33, no. 4, pp. 571, 2012.

[18] S. Vallaghé, M. Clerc, and J.-M. Badier, "In vivo conductivity estimation using somatosensory evoked potentials and cortical constraint on the source," in *Proc. IEEE 4th Int. Symp. Biomed. Imagi. (ISBI)*, Washington D.C., USA, 2007, pp. 1036–1039.

[19] S. Lew, C. H. Wolters, A. Anwander, S. Makeig, and R. S. MacLeod, "Improved EEG source analysis using low-resolution conductivity estimation in a four-compartment finite element head model," *Hum. Brain Mapp.*, vol. 30, no. 9, pp. 2862–2878, 2009.

[20] S. Lew, C. Wolters, A. Anwander, S. Makeig, and R. MacLeod, "Low resolution conductivity estimation to improve source localization," in *International Congress Series*. Elsevier, 2007, vol. 1300, pp. 149–152.

[21] F. Costa, H. Batatia, T. Oberlin, and J.-Y. Tourneret, "Bayesian Structured Sparsity Priors for EEG Source Localization Technical Report," Tech. Rep., University of Toulouse, ENSEEIHT, 2015.

[22] A. Gramfort, M. Kowalski, and M. Hämäläinen, "Mixed-norm estimates for the M/EEG inverse problem using accelerated gradient methods," *Phys. Med. Biol.*, vol. 57, no. 7, pp. 1937, 2012.

[23] T. F. Oostendorp, J. Delbeke, and D. F. Stegeman, "The conductivity of the human skull: results of in vivo and in vitro measurements," *IEEE Trans. Biomed. Eng.*, vol. 47, no. 11, pp. 1487–1492, 2000.

[24] G. Casella and C. P. Robert, *Monte Carlo Statistical Methods*, New York: Springer-Verlag, 1999.

[25] E. J. Candes, "The restricted isometry property and its implications for compressed sensing," *C. R. Académie des Sciences*, vol. 346, no. 9, pp. 589–592, 2008.

[26] A. Gramfort, M. Luessi, E. Larson, D. A. Engemann, D. Strohmeier, C. Brodbeck, L. Parkkonen, and M. S. Hämäläinen, "MNE software for processing MEG and EEG data," *NeuroImage*, vol. 86, pp. 446–460, 2014.

[27] A. Gramfort, M. Luessi, E. Larson, D. A. Engemann, D. Strohmeier, C. Brodbeck, R. Goj, M. Jas, T. Brooks, L. Parkkonen, et al., "MEG and EEG data analysis with MNE-Python," *Front. Neurosci.*, vol. 7, no. 267, pp. 1–13, 2013.

[28] S. P. Brooks and A. Gelman, "General methods for monitoring convergence of iterative simulations," *J. Comput. Graph. Statist.*, vol. 7, no. 4, pp. 434–455, 1998.